Characterizing the Effects of Al(OH)3 and Mg(OH)2 on Reaction Products and Drying Shrinkage Characteristics of Alkali-activated Slag

Li, Jing ; Yin, Suhong; Huang, Haoliang; Hu, Jie; Yi, Chaofan ; Chen, Zheng ; Ma, Yuwei; Ye, Guang

DOI
10.1016/j.cscm.2022.e01309

Publication date
2022

Document Version
Final published version

Published in
Case Studies in Construction Materials

Case Studies in Construction Materials 17 (2022) e01309

Contents lists available at ScienceDirect

Case Studies in Construction Materials

journal homepage: www.elsevier.com/locate/cscm

Characterizing the effects of $Al(OH)_3$ and $Mg(OH)_2$ on reaction products and drying shrinkage characteristics of alkali-activated slag

Jing Li [a,b], Suhong Yin [b,*], Haoliang Huang [b], Jie Hu [b], Chaofan Yi [a], Zheng Chen [a], Yuwei Ma [c], Guang Ye [d], Qijun Yu [b,*]

[a] Key Laboratory of Disaster Prevention and Structural Safety of China Ministry of Education, School of Civil Engineering and Architecture, Guangxi University, Nanning 530004, China
[b] School of Materials Science and Engineering, South China University of Technology, Guangzhou 510640, China
[c] Guangzhou University - Tamkang University Joint Research Center for Engineering Structure Disaster Prevention and Control, Guangzhou University, Guangzhou 510006, China
[d] Faculty of Civil Engineering and Geosciences, Delft University of Technology, 2628CN Delft, the Netherlands

ARTICLE INFO

Keywords:
Alkali-activated slag
Drying shrinkage
$Al(OH)_3$
$Mg(OH)_2$
Reaction products

ABSTRACT

This study is undertaken to explore the relationship between the reaction products and the drying shrinkage of alkali-activated slag (AAS) with the varying hydroxide dosage. AAS pastes were firstly produced with either $Al(OH)_3$ or $Mg(OH)_2$ to investigate the effects of hydroxide on the composition of reaction products and the drying shrinkage of AAS. Secondly, the main reaction products formed in AAS pastes, viz. C_4AH_{13}, M_4AH_{10}, C-S-H, C-A-S-H and C-M-S-H, were synthesized individually. Synthetic products were then taken to cast the respective paste sample to examine the performance against the drying exposure. The results show that adding $Mg(OH)_2$ indeed improved the shrinkage resistance of AAS. This is primarily connected to the increased crystalline phases, namely the hydrotalcite-like phases and the unreacted $Mg(OH)_2$. Whereas adding $Al(OH)_3$ did not relieve the drying shrinkage of AAS as the interlayer spacing of C-A-S-H was enlarged, which in turn allowed for more shrinkage. Further, the investigation of individual synthetic products illustrates that their drying shrinkage scales satisfied the following order: C_4AH_{13} < M_4AH_{10} < C-M-S-H < C-S-H < C-A-S-H. Moreover, the shrinkage scale of C-S-H was found to evolve as the Ca/Si ratio decreased.

1. Introduction

In 2020, the ordinary Portland cement (OPC) production in China was 2.395 billion tonnes [1,2]. Yet, the corresponding carbon footprint also reached about 1.384 billion tonnes [2], which had developed into a significant contributor to global warming. In the attempt to promote sustainable development, clinker-free cementitious materials have been attracting extensive scientific interest from researchers [3,4]. Alkali-activated slag (AAS) belongs to the family of alkali-activated materials and also has now gained broad attention, attributed to its high early strength [5], low permeability [6], excellent acid resistance [7] and low carbon emission [8]. However, the drying shrinkage found in AAS is 2–6 times as large as OPC systems [9,10]. Such a problem plants a potential threat to

* Corresponding authors.
E-mail addresses: shyinjob@163.com (S. Yin), imshyin@scut.edu.cn (Q. Yu).

https://doi.org/10.1016/j.cscm.2022.e01309
Received 8 May 2022; Received in revised form 20 June 2022; Accepted 8 July 2022
Available online 11 July 2022

structural safety and accordingly, limits the widespread application of AAS in the civil engineering field [11,12]. The mechanisms underlying the drying shrinkage of AAS have been investigated by prior studies. Collins et al. [13,14] recognized that the high capillary force caused by the finely porous nature alongside the high surface tension was mainly responsible for this durability issue in AAS. Besides, the reaction products of AAS also play an important role. The principal products formed in AAS are C-(A)-S-H gels, shrinkage-prone silica gels and a part of crystalline products, e. g. hydrotalcite-like phase [15,16]. The low proportion of crystalline phases decides that the AAS systems may be susceptible to the drying environment [17]. In this regard, Rashad et al. [18] found that adding quartz powders could significantly improve the shrinkage resistance of AAS, as these crystals may act as the micro-aggregates to fill in the voids. Thus, regulating the reaction products in AAS, especially crystal phases, appears to draw extensive scientific interest.

The oxides constituting the precursor strongly affect the composition of reaction products in AAS. Gong and White [19] noted that the composition of reaction products alongside the structure of C-(N)-A-S-H may be dependent on the MgO and Al_2O_3 contents. In addition, a secondary product, called the hydrotalcite-like phase, is usually formed in AAS specimens. Haha et al. [20] reported that increasing the MgO content in slag could promote the formation of hydrotalcite-like phases, while the Al/Si ratio of C-A-S-H was reduced. Raising the Al_2O_3 content in precursor was reported to reduce the Mg/Al ratio of the hydrotalcite-like phase [21]. Prior studies also reported that varying the chemical compositions of these reaction products could change the properties of AAS systems significantly. For instance, improving the crystal content was found to reduce the drying shrinkage [22], and increasing the hydrotalcite-like phase proportion indeed benefited the associated carbonation resistance [23]. As an industrial waste, the chemical composition of slag is strongly related to the raw material, viz. iron ore. However, the chemical compounds constituting iron ore are dominated by the local environment and, may not be possible to be adjusted per our subjective expectations. Thus, compared with regulating the chemical composition of slag, it is more feasible to modify the chemical composition of the precursor by integrating additives.

To address the above issue, Rashad [24] investigated the type of additives on the performances of sodium-sulfate activated slag. It was found that adding fly ash, limestone, hydrated lime and Portland cement would all help alleviate the drying shrinkage. Jin et al. [22] examined the drying shrinkage of AAS systems incorporating the reactive MgO. The results showed that the presence of MgO could react with water to form $Mg(OH)_2$ and in turn, triggered additional expansion. This volumetric expansion filled in the internal pores on the one hand and suppressed the subsequent shrinking on the other hand. Further, adding MgO was noticed to boost the formation of hydrotalcite-like phases, which may act as a skeleton and then relieve the drying shrinkage of AAS pastes [22,25]. Hamdy et al. [25] reported that introducing nano Al_2O_3 into AAS systems contributed to the formations of strätlingite and/or C_4AH_{13}, which eventually alleviated the drying shrinkage. Also, Ye et al. [26] noted that the sulfate-based expansive agent was more effective in reducing the shrinkage of AAS than the CaO-based expansive agent. Generally, the drying shrinkage occurring in AAS depends on both the content of crystal phases and the volume expansion sourced from the hydration of extra oxides. Yet, the relationship between the reaction products and the drying shrinkage of AAS is not clear enough, due to the interference of the hydration of oxides alongside the evolving pore structure. In this regard, adding hydroxide additives, such as $Mg(OH)_2$ and $Al(OH)_3$, maybe a more convenient way to improve the drying shrinkage characteristics of AAS systems.

Introducing $Mg(OH)_2$ and $Al(OH)_3$ may be the promising means to relieving the drying shrinkage of AAS systems. However, there so far exists very limited information to clarify the mechanisms underlying the effect of hydroxide additives on this common durability issue in AAS systems. Hence, the present study was undertaken to examine the relationships between the reaction products and the drying shrinkage of AAS pastes modified with $Mg(OH)_2$ and $Al(OH)_3$. A batch of AAS pastes was produced by activating the slag together with either $Mg(OH)_2$ or $Al(OH)_3$. It was followed by the drying shrinkage test accompanied by a suite of thermal, morphological, chemical, and microstructural investigations. In addition, the main reaction products comprising the AAS paste were synthesized individually, using the chemical precipitation technique. These products were then taken to produce the respective paste system and tested in a drying chamber to evaluate the shrinkage scale for each synthetic product. Through this study, it is hoped to offer a fresh view on controlling the drying shrinkage of AAS by regulating its mix design and reaction products.

2. Experimental program

2.1. Raw materials

2.1.1. Creation of AAS pastes

A commercially sourced slag with a specific surface area of 410 m^2/kg and a specific gravity of 2.85 g/cm^3 was used as the principal precursor to produce AAS specimens. The corresponding oxide constituents as determined by X-ray fluorescence (XRF) are presented in Table 1. Besides slag, crystalline $Al(OH)_3$ and $Mg(OH)_2$ were added separately to serve as the secondary precursor. The specific surface area of these two hydroxide crystals was 507 m^2/kg and 586 m^2/kg, while the associated specific gravity was 2.40 g/cm^3 and 2.36 g/cm^3, respectively. These raw materials were assessed under X-ray diffraction to evaluate their mineral phases, with the Cu-Kα radiation scanned from 5° to 70° alongside a step size of 0.013°. The obtained XRD patterns are illustrated in Fig. 1. As seen therein, the main

Table 1
Chief oxide constituents of employed slag and Portland cement.

Oxide (wt%)	CaO	SiO_2	Al_2O_3	MgO	Fe_2O_3	SO_3	others
Slag	40.23	34.86	15.07	5.10	0.89	2.11	1.74
Portland cement	65.68	21.04	5.32	1.84	3.50	0.44	2.18

mineral phases constituting this slag were amorphous, as evident from a smooth XRD trace with a tell-tale hump centered at about 30° [27]. Besides, a few weak crystal signals, assigned to akermanite and gismondine, were detected as well. As expected, the XRD traces of both $Al(OH)_3$ and $Mg(OH)_2$ exhibit significant crystal peaks attributed to the respective hydroxide compound. The sodium silicate solution was blended with the sodium hydroxide to produce the required activator with a modulus (SiO_2/Na_2O molar ratio) of 1.5. The mixing proportions for various AAS paste mixtures are listed in Table 2.

2.1.2. Synthesis of reaction products

Synthesizing reaction products has been widely recognized to be a feasible approach to investigate the influence of chemical compositions on the properties of cementitious matrix [28,29]. In this study, the main reaction products constituting AAS pastes, namely C-X-S-H (X: either Al or Mg or none), hydrotalcite-like phase, and calcium aluminate hydrate [30], were synthesized separately to examine the associated drying shrinkage scale. In this regard, $Ca(NO_3)_2.4H_2O$, $Mg(NO_3)_2.6H_2O$, $Al(NO_3)_3.9H_2O$, $NaAlO_2$, $Na_2SiO_3.5H_2O$, NaOH, and ultrapure water were used to artificially synthesize each of reaction products. All these employed chemical reagents were of analytical grade.

2.2. Preparation of specimens

2.2.1. AAS pastes

A reference AAS sample was cast first by activating the slag with the blended activator. Then, another two series were produced separately, with either $Al(OH)_3$ or $Mg(OH)_2$. The content of the hydroxide crystal was variously set as 3 wt%, 6 wt% and 10 wt%, in proportion to the amount of precursor. For all mixes, the Na_2O content and the water-to-solid ratio (*w/s*) ratio were respectively fixed at 6 wt% and 0.4, to eliminate the potential disturbance (see Table 2). Preceding the formal casting, slag experienced a dry stirring with hydroxide ($Al(OH)_3$ or $Mg(OH)_2$) in a VH015 V-shaped mixer for 2 h to yield the well-blended precursor. To produce the fresh AAS mixture, the pre-determined activator solution was firstly poured into the mixer and stirred for 30–60 s to ensure fair homogeneity. Then, the blended precursor was added and mixed for another 2 min. The obtained fresh mixture was thereafter cast into two sets of molds, sized as 25 mm × 25 mm × 280 mm and 40 mm × 40 mm × 40 mm. All freshly produced specimens were then compacted on the vibrating table [31,32]. 24 h later, the specimens were demolded and cured under the standard condition (T = 20 ± 2 ℃ and RH=90 ± 5%) for another 2 days. The prismatic specimens were retrieved for the drying shrinkage test, while the cubic specimens were used in the following thermal, morphological, chemical and microstructural characterizations. Of particular note, the obtained samples should be immersed in the anhydrous ethanol solution for 3 days to terminate the ongoing hydration as well as alkali-activation prior to characterizations. After that, they are dried in a vacuum chamber for 7 days, with the temperature set at

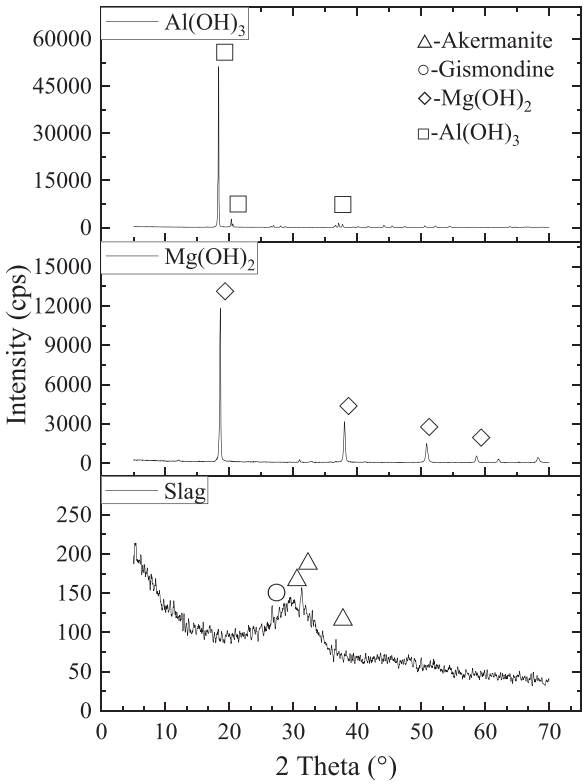

Fig. 1. XRD traces of raw slag and hydroxides.

Table 2
Mixing proportions of AAS pastes.

Specimens	Slag (g)	Al $(OH)_3$ (g)	Mg $(OH)_2$ (g)	Sodium silicate (g)	Na_2O (wt%)	w/s ratio[a]
S-0	100	0	0	50	6	0.4
S-Al3	100	3	0	51.5	6	0.4
S-Al6	100	6	0	53	6	0.4
S-Al10	100	10	0	55	6	0.4
S-Mg3	100	0	3	51.5	6	0.4
S-Mg6	100	0	6	53	6	0.4
S-Mg10	100	0	10	55	6	0.4

[a] w/s ratio = water to solid ratio by mass; solid=slag+ $Al(OH)_3$ +$Mg(OH)_2$ +Na_2O+ SiO_2.

60 ℃.

2.2.2. Synthetic products

The initial chemical compositions of synthetic products are presented in Table 3. Prior studies noticed the actual Ca/Si molar ratio of C-S-H may be lower than the designed value since the solubility of calcium in equilibrium solutions was slightly higher than that for silicate [33,34]. So that, the initial Ca/Si ratio designed for the C-S-H series is slightly higher than the expected value in this study. To synthesize C-S-H, C-A-S-H and C-M-S-H, calcium nitrate (0.67–1.5 mol/L), aluminum nitrate (0.02 mol/L) and magnesium nitrate (0.02 mol/L) solutions were added separately into the sodium silicate solution (0.1 mol/L). With regard to M_4AH_{10} (MAH-2 or hydrotalcite-like phase) and C_4AH_{13} (CAH-2 or calcium aluminate hydrate), they were respectively synthesized by adding 0.2 mol/L magnesium nitrate solution and 0.2 mol/L aluminum nitrate solution, into sodium metaaluminate solution (0.1 mol/L). During the synthesis, the mixed solutions were constantly stirred under the nitrogen atmosphere. Also, the pH value was fixed at about 13 to simulate the actual alkaline condition when producing AAS systems.

2.2.3. Pastes made with the synthetic product

The synthetic product was blended with 50 wt% of Portland cement to produce the respective paste specimen. The P•I 52.5 Portland cement with a specific surface area of 350 m^2/kg alongside a specific gravity of 3.10 g/cm^3 was employed to act as an auxiliary binder, as the lone synthetic product could not trigger any hydration. In addition, the water to solid ratio (*w/s*) was fixed at 0.62 for all mixes. The detailed mixing proportions are presented in Table 4. According to Chinese standard GB/T 17671-1999 [32], the synthetic product was blended with cement to experience 2 min of dry mixing, then followed by another 2 min of mixing after adding water. The obtained fresh mixture was then cast into the prismatic mold with dimensions of 15 mm × 15 mm × 170 mm. Again, the paste specimens were cured in the standard curing chamber (T = 20 ± 2 ℃ and RH=90 ± 5%) for up to 3 days.

2.3. Test protocols

2.3.1. Pore size distribution and reaction degree of AAS pastes

The pore structure of hardened AAS pastes, aged 3 days, was characterized via mercury intrusion porosimetry (MIP) using the instrument Auto Pore IV 9500 V1 with an aperture testing range of 0.003–1000 μm. The reaction degree of hardened AAS paste was evaluated by the selective dissolution method [35,36]. In this manner, the solvent comprising methanol and salicylic acid was prepared in advance, with the mass ratio fixed at 12:1. Then, 1 g of specimen powder was added to 60 ml solvent to stir for 2 h. The resulting suspension was thereafter filtered to obtain the residue, which was taken to experience the calcination at 1000 ℃ for 2 h and weighed as m_1. In the meanwhile, another 1 g specimen powder was calcined at 1000 ℃ for 2 h and recorded as m_0. Given this, the reaction degree (RD) of AAS could be quantified according to the following equation:

$$RD = \frac{(m_0 - m_1)}{m_0} \times 100\% \quad (1)$$

2.3.2. Phase identification and chemical composition of AAS pastes

The mineral phases in AAS pastes were assessed through XRD using a Copper-K radiation beam (operated at 40 kV and 44 mA) with

Table 3
Initial Ca/Si, Al/Si, Mg/Si, Mg/Al and Ca/Al molar ratios of synthetic products.

Specimens	Initial Ca/Si ratio	Initial Al/Si ratio	Initial Mg/Si ratio	Initial Mg/Al ratio	Initial Ca/Al ratio
CSH-0.64	0.7	0	0	0	0
CSH-0.96	1.1	0	0	0	0
CSH-1.18	1.5	0	0	0	0
CASH-0.14	1.1	0.2	0	0	0
CMSH-0.16	1.1	0	0.2	0	0
MAH-2	0	0	0	2.0	0
CAH-2	0	0	0	0	2.0

Table 4
Mixing proportions of pastes made with the synthetic products.

Specimens	Type of synthetic products	Synthetic product (g)	Cement (g)	w/s ratio
CSH-0.64	C-S-H	50	50	0.62
CSH-0.96	C-S-H	50	50	0.62
CSH-1.18	C-S-H	50	50	0.62
CASH-0.14	C-A-S-H	50	50	0.62
CMSH-0.16	C-S-H+M-S-H	50	50	0.62
MAH-2	Hydrotalcite-like phase	50	50	0.62
CAH-2	Calcium aluminate hydrate	50	50	0.62

a step size of 0.013°/s, from 5° to 70° diffraction angle (2θ). Also, the thermogravimetric analysis (TGA) was carried out in the temperature range of 30–1000 °C with a heating rate of 10 ℃/min under the N_2 atmosphere. ^{27}Al nuclear magnetic resonance (NMR, Avance III 400, Bruker, Fällanden, Zürich, Switzerland) was conducted to capture the structural ordering of reaction products in AAS. Preceding the further elementary characterization using the scanning electron microscope coupled with an energy dispersive spectroscope (SEM/EDS), the tested samples required a series of pre-processes. First, the collected broken species were polished by using an automatic grinding-polishing machine (Tegramin-25, Struers, Denmark), equipped with the abrasive paper of 500, 1200, 2000 and 4000 meshes. During this process, the applied pressure was constantly kept at 10 N and the anhydrous ethanol was used as the lubricant. Then, the obtained samples were washed and dried, prior to the further coating by gold. When observed under SEM/EDS, the instrumental parameters were set the same as previous. Further, 15 sample points were randomly selected from the scanned region to determine the elementary compositions.

2.3.3. *Characterizations of synthetic products*

The chemical compositions comprising synthetic products were determined through XRF, while the involved mineral phases were assessed by XRD. Due to the limitations of XRD analysis in evaluating amorphous phases, the synthetic gel, C-X-S-H (X: either Al or Mg or none), was further characterized using TGA. Note here that, the testing parameters for the above characterizations were once again set the same as previous. Moreover, FTIR and ^{27}Al NMR were also conducted to verify the synthesis of amorphous phases. Furthermore, the density of each synthetic product was measured, per Chinese standard GB/T 208–2014 [37].

2.3.4. *Drying shrinkage test*

To minimize the effect of autogenous shrinkage on drying shrinkage, the specimens were cured for 3 days in the standard curing chamber (T = 20 ± 2 ℃ and RH=90 ± 5%) according to the literature [9,31]. The paste specimens made either from the precursor (slag + hydroxides) or from the synthetic reaction product were placed in a drying chamber for up to 28 days, wherein the temperature and relative humidity were continuously set as 20 ± 2 ℃ and 50 ± 5%, respectively. The variation in dimensions was then recorded using a cement comparator, and the resulting shrinkage could be computed based on the following equation:

$$DS = \frac{L_n - L_0}{L_0} \times 10^{-3} \tag{2}$$

Wherein, DS denotes the drying shrinkage (mm/m); L_0 represents the initial length of examined specimen (mm); L_n is the measured length of the specimen after n days of exposure (mm).

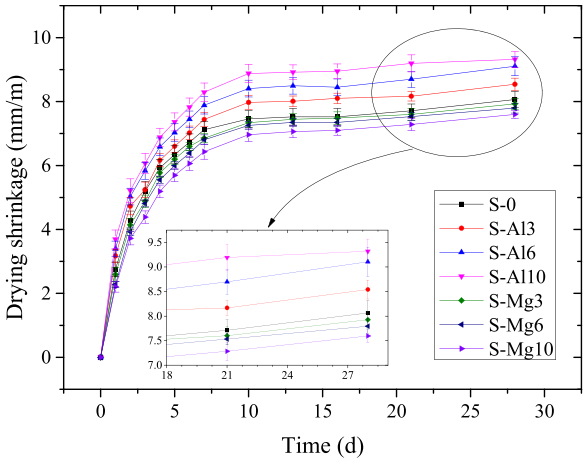

Fig. 2. Drying shrinkage of AAS pastes individually modified with $Al(OH)_3$ and $Mg(OH)_2$.

3. Results and discussions

3.1. Drying shrinkage of AAS pastes

Fig. 2 presents the drying shrinkage of AAS pastes modified by $Al(OH)_3$ and $Mg(OH)_2$. Clearly, the presence of $Al(OH)_3$ did not relieve the drying shrinkage of AAS pastes. More importantly, an increase in $Al(OH)_3$ content was even seen to intensify the shrinking in AAS pastes, as evident from the larger shrinkage scale for S-Al10 in comparison to the reference sample, S-0. On the contrary, the addition of $Mg(OH)_2$ was noted to improve the resistance of AAS to drying shrinkage. The shrinkage dropped from 8.1 mm/m to 7.6 mm/m as the $Mg(OH)_2$ content increased from 0 wt% to 10 wt%, corresponding to a 6.2% reduction. Similar benefits brought by crystal phases upon resisting drying shrinkage were witnessed elsewhere [18,22]. Rashad et al. [18] found adding 10% quartz powder would alleviate the drying shrinkage by 9.3% after 25 days, while Jin et al. [22] reported that introducing 7.5% medium reactive MgO reduced the drying shrinkage of AAS pastes by 13% after 90 days. However, it should be noticed here that although adding $Mg(OH)_2$ indeed relieved the drying shrinkage, the scale found for AAS examined here was greater than that for typical OPC systems [10,12]. Specifically, the drying shrinkage of OPC exposed under the relative humidity of 50% for 28 days was reported as ~4 mm/m [12], which was only about 53% of AAS systems. Therefore, besides adding crystal phases, other approaches are strongly required to solve the shrinkage issue of AAS when applied in practical applications. Furthermore, the obtained results reveal that the AAS systems shrunk fast within the first 10 days of drying exposure, and the further exposure displayed a convergent trend. This implies that in practical engineering, any measures adopted to relieve the drying shrinkage should be carried out within this reported period.

3.2. Reaction degree and microstructural characterizations for AAS pastes

The reaction degree of various AAS pastes is presented in Fig. 3. As seen therein, the examined AAS pastes display the close reaction degree. This indicates that regardless of dosage, the presence of $Al(OH)_3$ or $Mg(OH)_2$ would not affect the reaction rate of AAS pastes considerably. Three representative paste systems, namely S-0, S-Al6 and S-Mg6, were characterized further by MIP. The total porosity and the incremental porosity are illustrated in Fig. 4. Again, these three AAS systems register the approximate porosities, which are 22.4% for S-0, 23.1% for S-Al6, and 22.3% for S-Mg6. Also, the critical pore sizes of these three specimens are found as 9.05 nm, 7.23 nm, and 9.05 nm, respectively. The obtained MIP results may indicate that the effect of microstructure on the drying shrinkage of AAS modified with hydroxides was limited.

3.3. Mineral, thermal gravimetric and chemical characterizations of AAS pastes

Fig. 5 presents the XRD patterns of AAS pastes made with hydroxides. Clearly, the chief reaction product in AAS paste was C-(A)-S-H. Besides, minor signals ascribed to hydrotalcite-like phase and calcium aluminate hydrate were detected. When compared to the reference mix, i. e. S-0, additional peaks indicating $Al(OH)_3$ or $Mg(OH)_2$ were respectively observed in S-Al and S-Mg series. Also, the intensity of these crystal signals evolved as the hydroxide content increased. This may imply that $Al(OH)_3$ or $Mg(OH)_2$ rarely participated in the chemical reactions.

The TG/DTG curves of AAS pastes are shown in Fig. 6. Three major peaks could be observed as the temperature progressively varies from 30 ℃ to 235 ℃, from 235 ℃ to 320 ℃, and from 320 ℃ to 430 ℃. The first weight loss occurring between 30 ℃ and 235 ℃ is mainly due to the dehydration of C-(A)-S-H and M-S-H [15,22]. Of particular note, these two products are amorphous phases formed in the alkali-activation of slag. For the following two peaks, the one located at 235–320 ℃ is attributed to decompositions of $Al(OH)_3$ and calcium aluminate hydrate, while the decomposed $Mg(OH)_2$ and the hydrotalcite-like phase collaboratively caused the weight loss occurring in 320–430 ℃. The cumulative weight loss for each specimen was calculated to quantify the influence of $Al(OH)_3$ and $Mg(OH)_2$ on reaction products of AAS, as now presented in Fig. 7. Compared with the reference group S-0, while the S-Al series lost much less weight due to the dehydration of amorphous phases, more weight loss due to the evaporation of chemically bound water

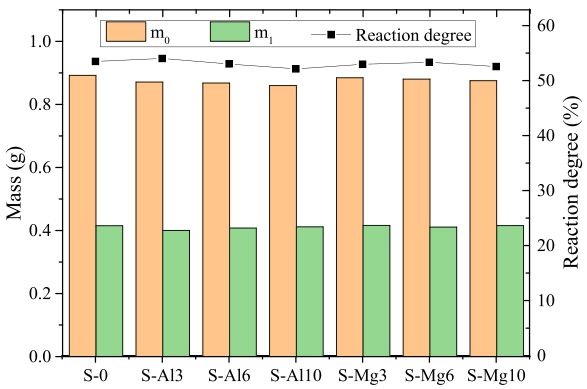

Fig. 3. Reaction degree of various AAS pastes.

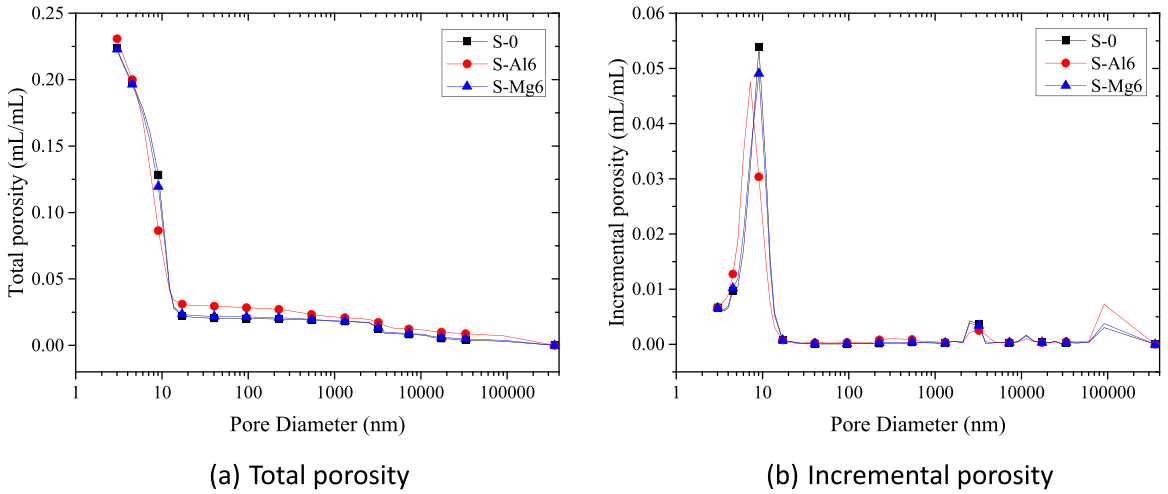

Fig. 4. Pore size distribution of AAS pastes after curing for 3 days.

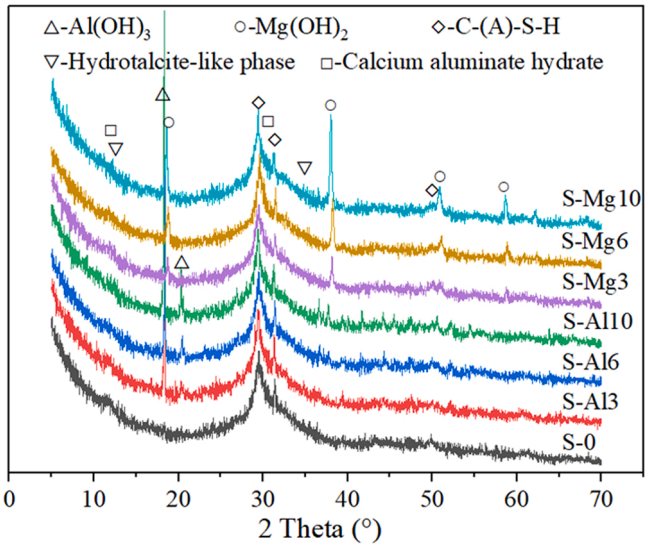

Fig. 5. XRD traces of AAS pastes.

constituting crystal compounds could be found. This implies that limited $Al(OH)_3$ participated in the chemical reactions to form C-(A)-S-H. By contrast, the presence of $Mg(OH)_2$ did not suppress the formation of those amorphous phases. Especially, the AAS paste incorporating 3% $Mg(OH)_2$ was seen to achieve slightly more amorphous reaction phases than S-0, as evident from Fig. 7.

Specimens S-0, S-Al6, and S-Mg6 were taken for ^{27}Al NMR measurement. Fig. 8 reveals the ^{27}Al NMR spectra alongside the deconvolution profiles for these three representative samples. The peaks resonating at about 10 ppm, 40 ppm, and 65 ppm indicate the six-coordinated Al[VI], the five-coordinated Al[V] and the four-coordinated Al[IV], respectively [38–44]. The peaks centered at 66 ppm and 74 ppm are respectively assigned to the four-coordinated aluminum at the pairing position and cross-linked position in C-A-S-H ([IV]-Q^2 and [IV]-Q^3) [38–40]. In addition, the four-coordinated Al [IV] resonating at 58 ppm is sourced from the unreacted slag (Al[IV]-S) [38]. The deconvolution peaks centered at 5 ppm and 10 ppm are related to the six-coordinated aluminum, which is respectively carried by the third aluminate hydrate (TAH, Al [VI]-T) and $Al(OH)_3$ (Al[VI]-A) [41]. As well, the Al[VI] incorporated in the hydrotalcite-like phase (Al[VI]-H) and calcium aluminate hydrate (Al [VI]-C) may be captured at 10–13 ppm after the deconvolution process [42–44]. Table 5 summarizes the detailed data in terms of types of aluminum coordination. The corresponding content is quantified based on the chemical compositions of raw materials, as shown in Fig. 9. As compared to the reference (S-0), the S-Al6 group contains more TAH (Al[VI]-T) and unreacted $Al(OH)_3$ (Al[VI]-A). On the other hand, the S-Mg6 system registers a minor reduction in Al[VI]-T and Al[IV] amounts, whereas the corresponding formation of Al[VI]-H/C is increased slightly.

As widely reported, the Al/Si ratio dominates the properties of alkali-activated systems as it is essentially connected to the polymerization degree of the silica chain in C-(A)-S-H [45]. Hence, the Al/Si and Mg/Si ratios were measured for AAS pastes in SEM/EDS. A

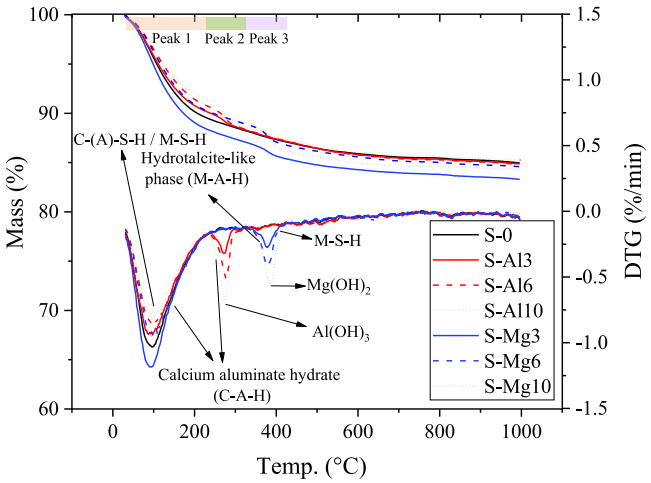

Fig. 6. TG/DTG curves of AAS pastes.

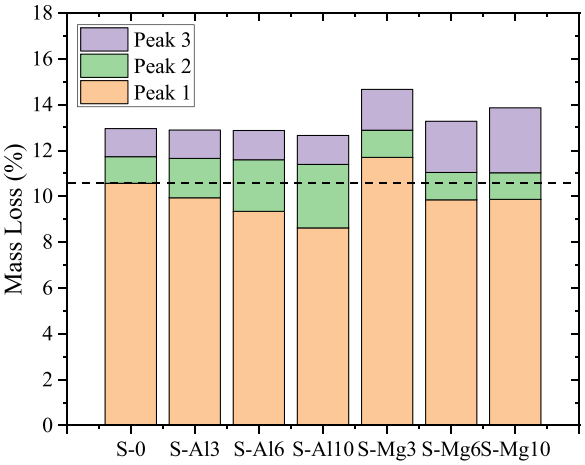

Fig. 7. Calculated weight loss of AAS pastes related to each peak in TGA.

linear fitting process is carried out to calculate the Al/Si ratio of C-(A)-S-H, according to the associated intercept with the x-axis [22, 46]. As well, the Mg/Al ratio of the hydrotalcite-like phase can be determined from the slope [22,46]. The obtained fitting curves for AAS specimens are shown in Fig. 10. The slope and the intercept with the x-axis are listed in Table 6. Clearly, an increase in $Al(OH)_3$ content corresponds to a reduction in the Mg/Al molar ratio of the hydrotalcite-like phase but a rise in the Al/Si molar ratio of C-(A)-S-H. Yet, adding $Mg(OH)_2$ is seen to decrease the Al/Si molar ratio of C-(A)-S-H. Given these, the addition of $Al(OH)_3$ may boost the transformation of C-S-H into C-A-S-H. Secondly, the S-Al series is noted to contain more TAH (Al[VI]-T) according to the ^{27}Al NMR results. These two reasons together explain the reduced Mg/Al ratio of the hydrotalcite-like phase in presence of $Al(OH)_3$. On the other hand, when Mg content is abundant, Al preferentially forms the hydrotalcite-like phase, instead of C-S-H [22].

As summarized above, although the addition of hydroxides generated a minor influence on the microstructure of AAS, these crystals play some parts in controlling the composition of reaction products. To explore the relationship between the composition of reaction products and the drying shrinkage of AAS pastes made with $Al(OH)_3$ or $Mg(OH)_2$, the shrinkage scale measured at 28 days, the weight loss of crystal phases and the Al/Si molar ratio of C-(A)-S-H are plotted as a function of the hydroxide content in Fig. 11. Clearly, when increasing the $Mg(OH)_2$, the content of crystalline phases in AAS increases whereas the Al/Si molar ratio of C-(A)-S-H drops. This eventually corresponds to the alleviated drying shrinkage. On the other hand, increasing the $Al(OH)_3$ content is seen to improve the Al/Si ratio of C-(A)-S-H and the content of crystalline phases. However, the corresponding drying shrinkage is enlarged. Given this, it may be speculated that lowering the Al/Si molar ratio of C-(A)-S-H is crucial for AAS paste to resist the drying shrinkage.

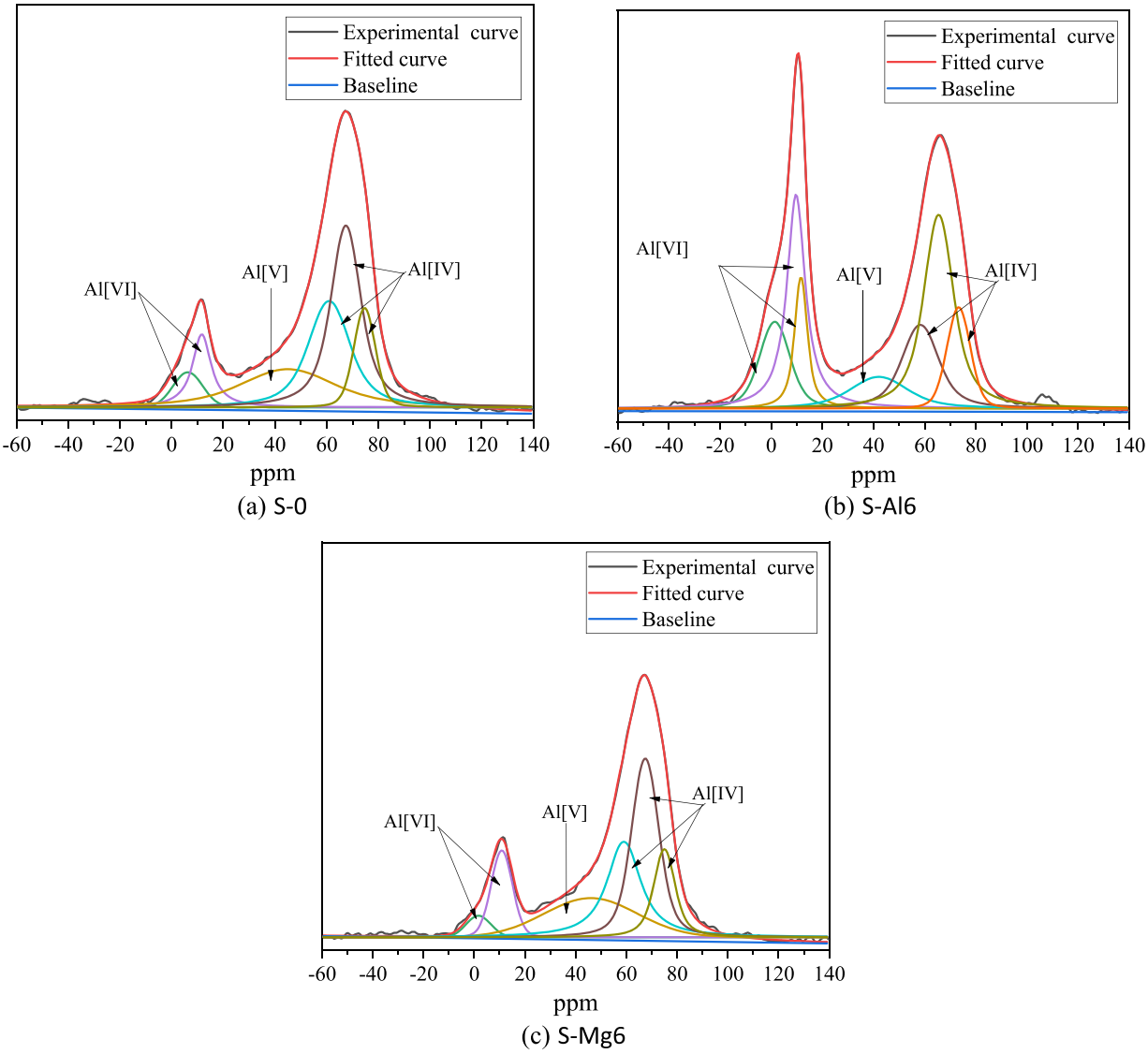

Fig. 8. ^{27}Al NMR spectra of AAS pastes: (a) S-0, (b)S-Al6, and (c) S-Mg6.

3.4. Validation of synthetic reaction products

Recall earlier, the main reaction products in AAS systems were synthesized separately. Fig. 12 presents the density and the actual compositional ratios of these synthetic products. Comparing CSH-0.96, CASH-0.14 and CMSH-0.16, the existence of Al reduced the density, whereas the presence of Mg yielded an increase. Besides, for the other two synthetic products (the hydrotalcite-like phase (MAH-2) and the calcium aluminate hydrate (CAH-2)), the Mg/Al and Ca/Al ratios were respectively determined as 2.02 and 2.03, which both agreed with their designed values.

Fig. 13 displays the XRD patterns of synthetic products. The diffraction peak assigned to C-S-H could be observed in all C-(M)-(A)-S-H series [31,47,48]. With regard to CAH-2 and MAH-2, the peaks related to the hydrotalcite-like phase and the calcium aluminate hydrate are also detected, respectively. The above XRD results confirm the successful synthesis of crystal products.

The DTG curves of synthetic C-(M)-(A)-S-H are shown in Fig. 14. Clearly, all specimens display two significant weight losses as heating from the room temperature to 1000 ℃. The first one occurs in the range of 30–200 ℃, which is related to the dehydration of C-(A)-S-H or C-(M)-S-H [22,46]. And the second one is seen between 600 ℃ and 900 ℃, due to the decomposition of calcium carbonate [49]. In addition, CMSH-0.16 registers an additional peak at 350–430 ℃, attributed to the decomposition of magnesium silicate hydrate (M-S-H) [50]. This thermal gravimetric analysis reveals that the synthetic CMSH-0.16 sample is a blended product comprising both C-(M)-S-H and M-S-H.

The FTIR results for CSH-0.64, CSH-0.96 and CSH-1.18 are shown in Fig. 15. The vibration of Si-O-Si is found at about 450 cm^{-1}.

Table 5
Proportions of Al with different coordination numbers in AAS pastes.

Samples	Al[Ⅵ]-T		Al[Ⅵ]-A		Al[Ⅵ]-H/C		Al[Ⅴ]		Al[Ⅳ]-S		Al[Ⅳ]-Q2		Al[Ⅳ]-Q3	
	ppm	%	ppm	%	ppm	%	ppm	%	ppm	%	ppm	%	ppm	%
S-0	6.29	4.55	/	/	12.51	8.93	44.47	20.12	60.14	24.56	66.54	31.55	74.38	10.29
S-Al6	2.08	11.14	10.62	21.32	12.06	8.26	42.02	8.30	57.73	13.82	64.00	27.80	73.02	9.36
S-Mg6	1.74	2.85	/	/	11.00	10.36	45.96	19.43	58.12	24.42	66.99	31.38	74.31	11.57

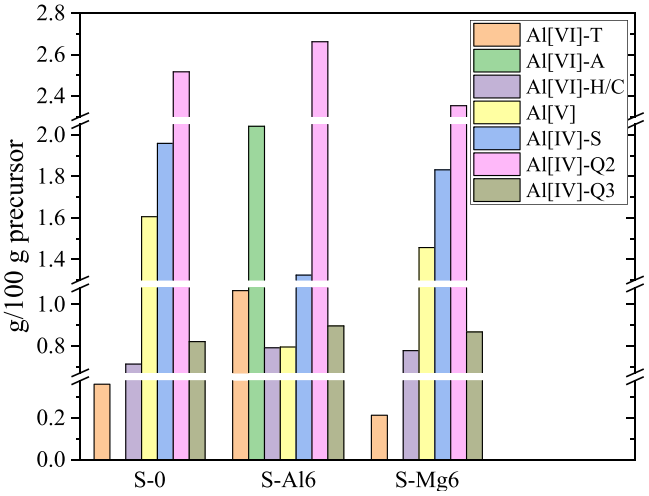

Fig. 9. Deconvolution results of ^{27}Al NMR.

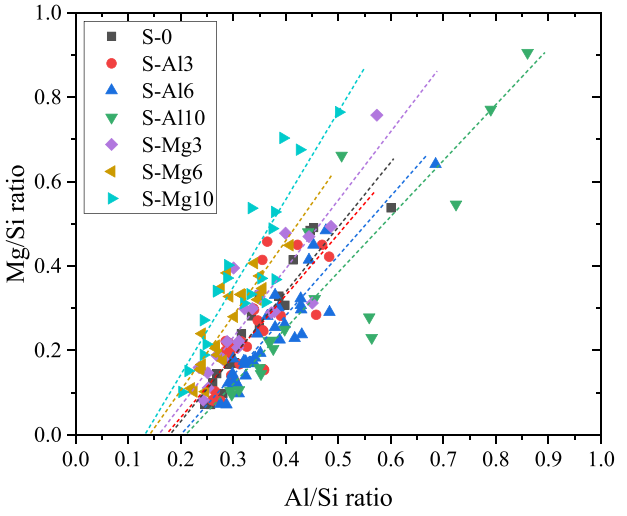

Fig. 10. Experimental data of SEM/EDS and the correlation between Mg/Si and Al/Si ratios in AAS pastes.

Table 6
Fitting equations and the associated intercept on the x-axis.

Specimens	Equations	Intersection with x-axis
S-0	Mg/Si = 1.54253 Al/Si − 0.27609	0.17899
S-Al3	Mg/Si = 1.45224 Al/Si − 0.25146	0.17315
S-Al6	Mg/Si = 1.41843 Al/Si − 0.29224	0.20603
S-Al10	Mg/Si = 1.25712 Al/Si − 0.25754	0.20487
S-Mg3	Mg/Si = 1.61714 Al/Si − 0.25862	0.15992
S-Mg6	Mg/Si = 1.80619Al/Si − 0.26135	0.14470
S-Mg10	Mg/Si = 2.08094 Al/Si − 0.27963	0.13438

Also, the peaks centered at 850 cm^{-1} and 970 cm^{-1} are respectively assigned to the Si-O band in Q^1 and Q^2 sites [49]. These characteristic peaks are found in all CSH series, which indicates the successful synthesis of C-S-H. Further, the wavenumber of the Si-O band in Q^2 site shifts towards the larger end as the Ca/Si ratio decreases. This implies a higher degree of polymerization of the associated silicon chain. The XRD results also report that the diffraction peak located at about 7° ($d_{(002)}$) moves towards the larger side of 2θ as the initial Ca/Si ratio decreases (see Fig. 13). Taken together, it may be speculated that the bridging silicon content in C-S-H gels is increased [31,47,48].

^{27}Al NMR is conducted to confirm the uptake of the Al atom by C-S-H and the formation of C-A-S-H. According to Fig. 16, the ^{27}Al

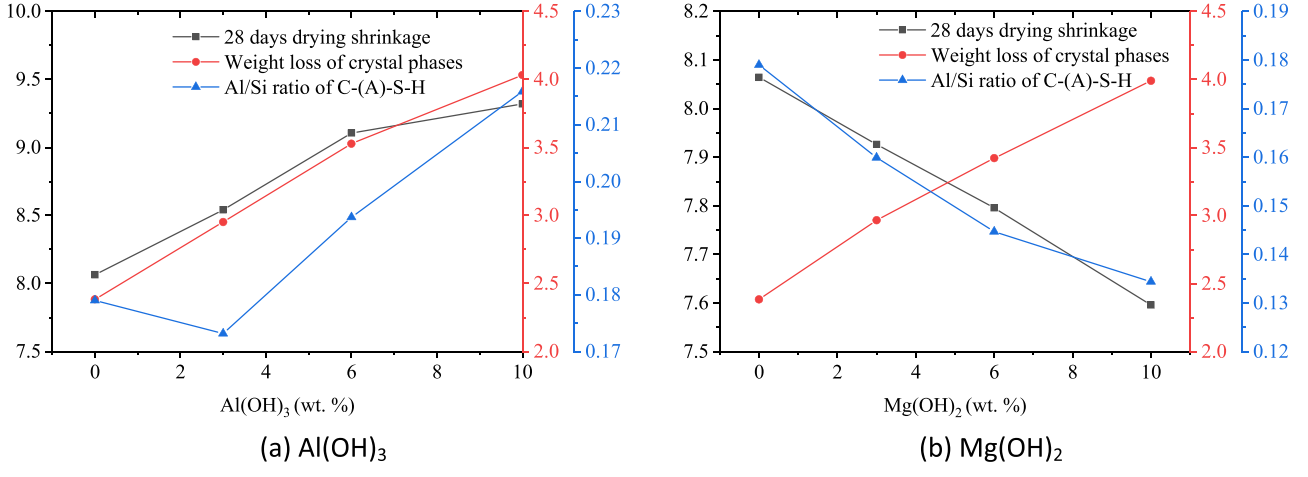

Fig. 11. Effect of (a) $Al(OH)_3$ and (b) $Mg(OH)_2$ on the composition of reaction products and drying shrinkage of AAS pastes.

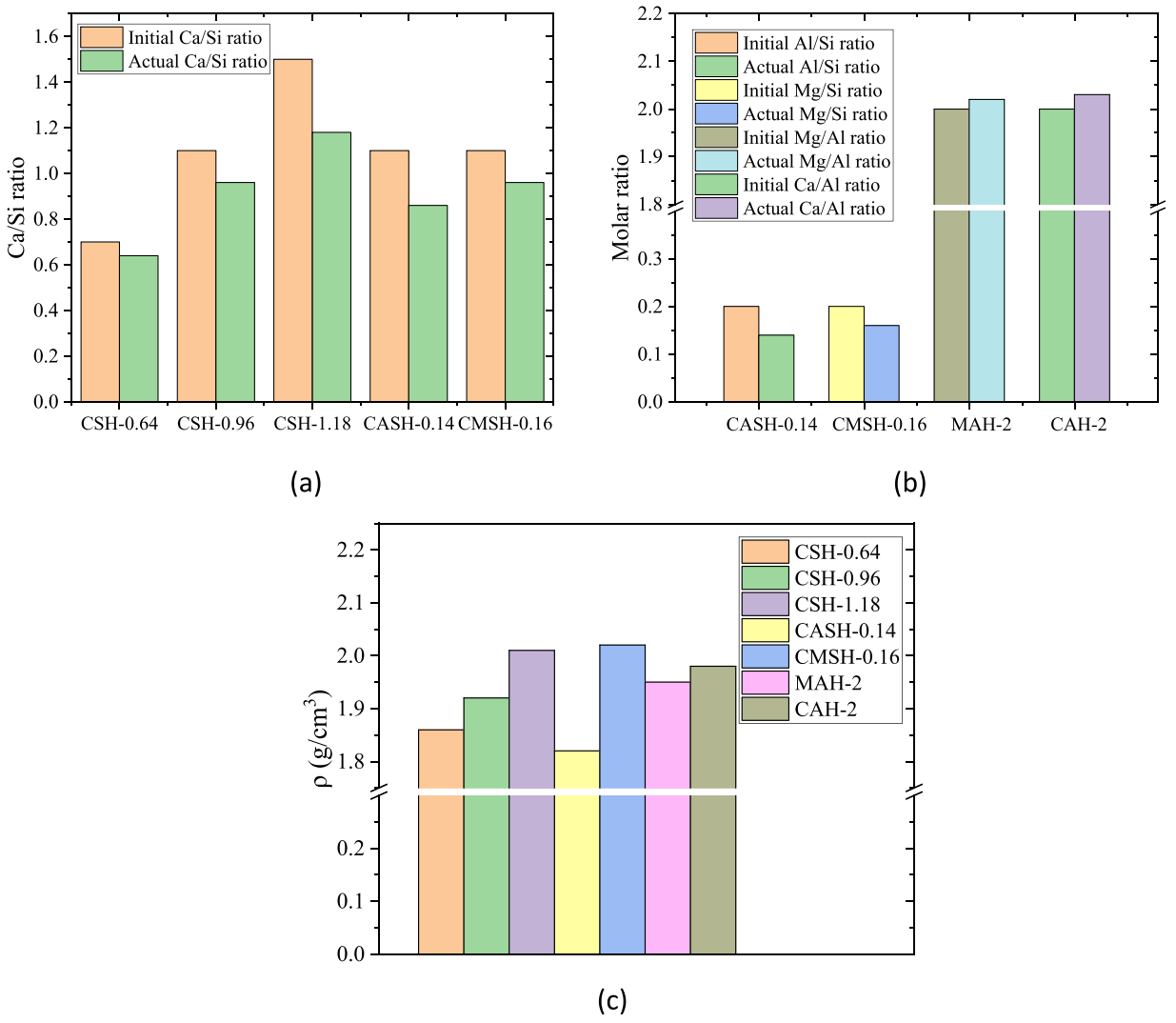

Fig. 12. Actual compositional ratios and the associated density of synthetic products.

NMR spectrum of synthetic CASH-0.14 possesses a resonation peak at about 70 ppm, assigned to the four-coordinated aluminum [48, 50]. This kindly confirms that the aluminum has now entered into the pairing or bridging tetrahedron, and the C-A-S-H is so synthesized. Note further, the aluminum at the position of the bridging tetrahedron has been found to increase the mean basal spacing (d_{002}), see Fig. 13. This was also reported elsewhere [31,35].

3.5. *Drying shrinkage of synthetic products*

The drying shrinkage of pastes produced with synthetic products is plotted in Fig. 17. Besides, a plain cement paste was also tested as the reference group. One can see that except for the reference group, all pastes made with the synthetic reaction product exhibit the viscous trait within the first 2 days of exposure. This manifests firstly in an increase in the slope of the drying shrinkage curve at the early stage, then followed by a decrease as time elapses [12,51]. Further, the pastes made with synthetic products all suffered more seriously from the drying exposure than the reference group, as evident from Fig. 17. This is mainly attributed to that the texture of the synthetic product is much less compact in comparison to the conventional cement mixture. As reported earlier in Fig. 12(c), the density of synthetic products is only 1.8–2.0 g/cm^3, whereas this value for Portland cement reaches up to 3.1 g/cm^3.

As for the CSH series, an increase in Ca/Si ratio seems to improve the shrinkage resistance, as evident from the lowest shrinkage scale detected for CSH-1.18. Recall Fig. 13, the diffraction angle assigned to $d_{(002)}$ shifts from 5.3° to 7.1° as the Ca/Si ratio increases from 0.64 to 1.18. Also, the interlayer spacing of C-S-H drops from 16.6 Å to 12.5 Å. Besides, a greater density is found for the specimen incorporating the larger Ca/Si ratio, see Fig. 12(c). The above results imply that an increase in the Ca/Si ratio has the potential to promote the compactness of C-S-H gels. As a result, the allowable space is reduced for the shrinkage of C-S-H.

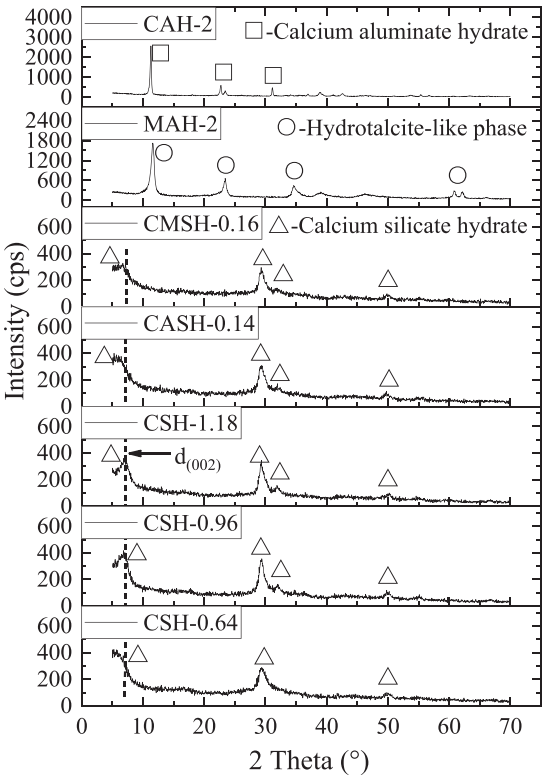

Fig. 13. XRD patterns of synthetic products.

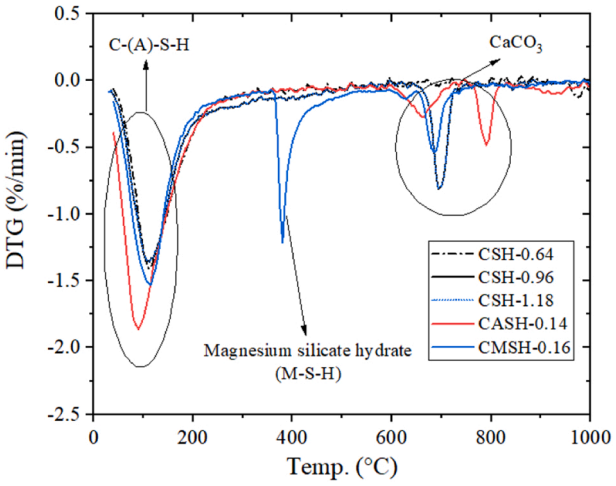

Fig. 14. DTG curves of synthetic products.

The transformation of C-S-H into C-A-S-H corresponds to a reduced diffraction angle assigned to $d_{(002)}$, as shown in Fig. 13. This indicates that C-A-S-H registers a larger interlayer spacing to accommodate the deformation. Therefore, the paste specimen made with CASH-0.14 is noted to shrink more significantly than that produced with CSH-0.96, as evident from Fig. 17. By contrast, the shrinkage of CMSH-0.16 is much smaller than CSH-0.96. This may be connected to the structural trait of the mixture of C-S-H and M-S-H. As well reported, C-S-H registers a layer structure [36], while the network of M-S-H is three-dimensional [52]. The former embedded into the latter may yield a much denser structure. This is supported by Fig. 12(c) that the CMSH-0.16 displays a greater density than CSH-0.96. Further, the specimens made with synthetic MAH-2 and CAH-2 are witnessed to experience the least shrinkage across all examined mixes, see Fig. 17. This may confirm the superior volumetric stability of crystal products.

As for the S-Al series, adding $Al(OH)_3$ contributes to the formation of calcium aluminate hydrate and also increases the Al/Si ratio of

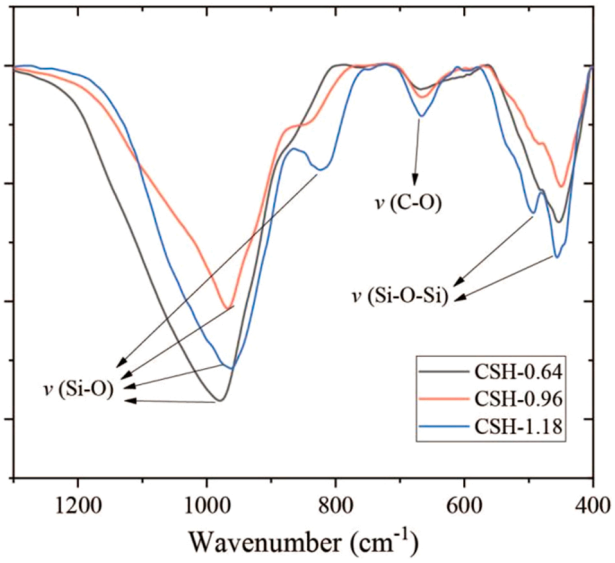

Fig. 15. FTIR spectra of synthetic C-S-H with varying Ca/Si molar ratio.

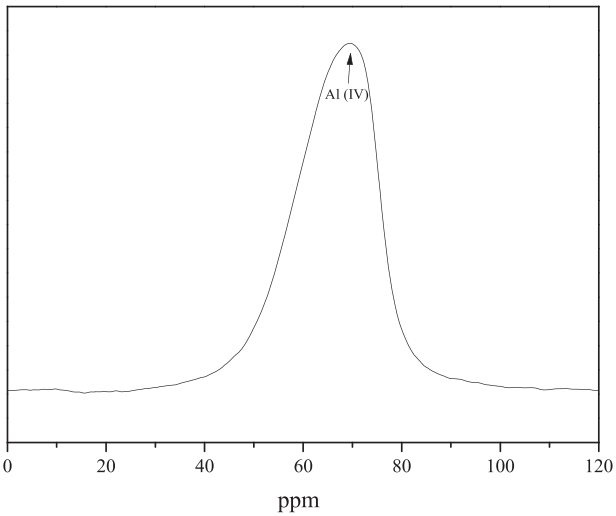

Fig. 16. ^{27}Al NMR spectrum of CASH-0.14.

C-(A)-S-H. While the former imparts good volumetric stability to the pastes, the latter deteriorates the shrinkage resistance of the pastes instead. Since the C-(A)-S-H is the predominant mineral constituting the AAS system, the associated influence is more significant and therefore dominates the eventual shrinkage characteristics of produced AAS specimen. Ye et al. [12] also reported that the reconstruction of C-(A)-S-H during the drying environment was responsible for the high shrinkage of AAS. Hence, the drying shrinkage evolved with an increase in the $Al(OH)_3$ content in this study. With regard to the S-Mg series, the presence of $Mg(OH)_2$ hinders the Al uptake by C-S-H and lowers the associated Al/Si ratio of C-(A)-S-H. Moreover, the presence of $Mg(OH)_2$ boosts the formations of hydrotalcite-like crystals and M-S-H [15,23], which subsequently improve the resistance of AAS against drying shrinkage.

4. Concluding remarks

This study aims to explore the relationships between reaction products and drying shrinkage of alkali-activated slag modified with hydroxides. Firstly, AAS pastes incorporating either $Al(OH)_3$ or $Mg(OH)_2$ were produced to investigate their microstructure, compositions of reaction products and drying shrinkage. The results reveal that the addition of hydroxides could affect the composition of reaction products in AAS and in turn, dominate the further shrinkage characteristics. Secondly, the principal reaction products in AAS were synthesized individually and then, blended with 50% Portland cement to cast the respective paste. These specimens were taken for the drying shrinkage test to evaluate the contribution of each reaction product to the drying shrinkage of AAS. Based on the

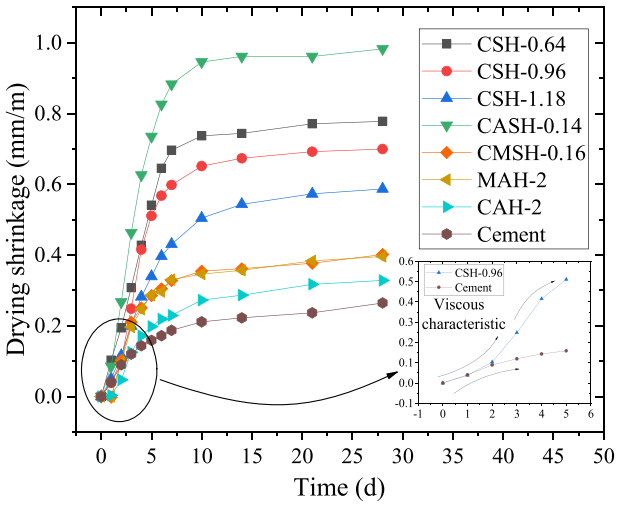

Fig. 17. Drying shrinkage of pastes made with varying synthetic products.

obtained results, the following conclusions may be drawn:

- The C-A-S-H displayed the greatest interlayer spacing among all synthetic products, which accordingly allowed for the most shrinkage. Increasing the content of $Al(OH)_3$ may improve the Al/Si ratio of C-A-S-H and in turn, weakened the resistance of AAS pastes to drying shrinkage.
- Adding $Mg(OH)_2$ reduced the Al/Si ratio of C-(A)-S-H on the one hand and increased the contents of the hydrotalcite-like phase and unreacted $Mg(OH)_2$ on the other hand. These collaboratively alleviated the drying shrinkage in AAS pastes.
- The contribution of synthetic products to drying shrinkage satisfied the following order: CAH-2 < MAH-2 < CMSH-0.16 < CSH series < CASH-0.14. The superior shrinkage resistance of CAH-2 and MAH-2 was essentially due to the crystal nature and the resulting excellent volumetric stability.
- The drying shrinkage of C-S-H could be relieved by increasing the Ca/Si molar ratio. This is mainly attributed to that the high Ca/Si ratio could reduce the interlayer spacing of C-S-H and the allowable space for shrinking.
- The CMSH-0.16 was found as a hybrid system comprising both M-S-H and C-S-H. The structural traits of these two sub-products may allow themselves to mutually coalesce and result in a more compact structure. This eventually manifested in an enhancement upon the shrinkage resistance. The CASH-0.14, transforming from C-S-H, possessed the enlarged interlayer spacing and the reduced density. Accordingly, the corresponding shrinkage scale ranked first across all synthetic products.

Declaration of Competing Interest

The authors declare the following financial interests/personal relationships which may be considered as potential competing interests: Jing Li reports financial support was provided by Guangxi Science and Technology Department. Suhong Yin, Jing Li reports financial support was provided by National Natural Science Foundation of China. The authors confirm that there is NO conflict of interest associated with this manuscript.

Data availability statement

The raw/processed data required to reproduce these findings cannot be shared at this time as the data also forms part of an ongoing study.

Acknowledgment

The present authors acknowledge the Guangxi Science and Technology Department (2021GXNSFBA075014 and AD21238007) and the National Natural Science Foundation of China (52108199 and 51561135012) for their financial support.

References

[1] National Bureau of Statistics, PRC. China Statistical Yearbook [M]. Beijing: China Statistical Press, 2021.
[2] https://new.qq.com/omn/20220426/20220426A0BBIS00.html.
[3] A. Mehta, R. Siddique, An overview of geopolymers derived from industrial by-products, Constr. Build. Mater. 127 (30) (2016) 183–198.
[4] I. Amer, M. Kohail, M.S. El-Feky, et al., A review on alkali-activated slag concrete, Ain Shams Eng. J. 12 (2) (2021) 1475–1499.
[5] Y. Ding, J.G. Dai, C.J. Shi, Mechanical properties of alkali-activated concrete: a state-of-the-art review, Constr. Build. Mater. 127 (2016) 68–79.

[6] Z. Zhang, H. Wang, Analysing the relation between pore structure and permeability of alkali-activated concrete binders. Handbook of Alkali-Activated Cements, Mortars and Concretes, 2015, pp. 235–264.
[7] C. Shi, Corrosion resistance of alkali-activated slag cement, Adv. Cem. Res. 15 (2) (2003) 77–81.
[8] P. Duxson, J.L. Provis, G.C. Lukey, et al., The role of inorganic polymer technology in the development of "green concrete", Cem. Concr. Res. 37 (12) (2007) 1590–1597.
[9] R.J. Thomas, D. Lezama, S. Peethamparan, On drying shrinkage in alkali-activated concrete: Improving dimensional stability by aging or heat-curing, Cem. Concr. Res. (2016) 91.
[10] C. Cartwright, F. Rajabipour, Aleksandra Radlińska, Shrinkage characteristics of alkali-activated slag cements, J. Mater. Civ. Eng. 27 (7) (2014) B4014007.
[11] H. Ye, C. Cartwright, F. Rajabipour, et al., Understanding the drying shrinkage performance of alkali-activated slag mortars, Cem. Concr. Compos. (2017) 13–24.
[12] H. Ye, A. Radlińska, Shrinkage mechanisms of alkali-activated slag, Cem. Concr. Res. 88 (2016) 126–135.
[13] F. Collins, J.G. Sanjayan, Effect of pore size distribution on drying shrinking of alkali-activated slag concrete, Cem. Concr. Res. 30 (9) (2000) 1401–1406.
[14] A. Tehmina, K.S. Ullah, M.F. Ahmed, Mechanical characteristics of hardened concrete with different mineral admixtures: a review, Sci. World J. 2014 (2014), 875082.
[15] H.A. Abdel-Gawwad, S. Abd El-Aleem, Effect of reactive magnesium oxide on properties of alkali activated slag geopolymer cement pastes, Cearmics 59 (1) (2015) 37–47.
[16] Kutti T., Berntsson L., Chandra S., Shrinkage of cements with high content of blast-furnace slag, Proceedings of Fly ash, silica fume, slag and natural pozzolans in concrete[J]. Istanbul, 1992. 615–625.
[17] B. Zhang, H. Zhu, Y. Cheng, et al., Shrinkage mechanisms and shrinkage-mitigating strategies of alkali-activated slag composites: a critical review, Constr. Build. Mater. 318 (2022), 125993.
[18] A.M. Rashad, D.M. Sadek, M. Gharieb, Valorization of quartz powder for drying shrinkage and carbonation resistance of alkali-activated slag cement, Environ. Sci. Pollut. Res. (2022) 1–13.
[19] K. Gong, C.E. White, Impact of chemical variability of ground granulated blast-furnace slag on the phase formation in alkali-activated slag pastes, Cem. Concr. Res. 89 (2016) 310–319.
[20] M.B. Haha, B. Lothenbach, G.L. Le Saout, et al., Influence of slag chemistry on the hydration of alkali-activated blast-furnace slag—Part I: effect of MgO, Cem. Concr. Res. 41 (9) (2011) 955–963.
[21] M.B. Haha, B. Lothenbach, G.L. Saout, et al., Influence of slag chemistry on the hydration of alkali-activated blast-furnace slag - Part II: Effect of Al_2O_3, Cem. Concr. Res. 42 (1) (2012) 74–83.
[22] F. Jin, K. Gu, A. Al-Tabbaa, Strength and drying shrinkage of reactive MgO modified alkali-activated slag paste, Constr. Build. Mater. 51 (2014) 395–404.
[23] S.A. Bernal, R.S. Nicolas, R.J. Myers, et al., MgO content of slag controls phase evolution and structural changes induced by accelerated carbonation in alkali-activated binders, Cem. Concr. Res. (2014) 57.
[24] A.M. Rashad, Influence of different additives on the properties of sodium sulfate activated slag, Constr. Build. Mater. 79 (2015) 379–389.
[25] A. Hamdy, Abdel Gawwad, S. Mona, et al., Mohammed Single and dual effects of magnesia and alumina nano-particles on strength and drying shrinkage of alkali activated slag, Constr. Build. Mater. 228 (2019), 116827.
[26] H. Ye, A. Radlińska, Shrinkage mitigation strategies in alkali-activated slag, Cem. Concr. Res. 101 (2017) 131–143.
[27] S.D. Wang, K.L. Scrivener, Hydration products of alkali activated slag cement, Cem. Concr. Res. 25 (3) (1995) 561–571.
[28] J. Li, D. Cao, S. Nong, et al., Solid solubility of magnesium oxide in aluminoferrite, Adv. Cem. Res. 5 (28) (2016) 336–343.
[29] T.F. Sevelsted, J. Skibsted, Carbonation of C–S–H and C–A–S–H samples studied by ^{13}C 27Al and 29Si MAS NMR spectroscopy, Cem. Concr. Res. 71 (2015) 56–65.
[30] W. Chen, H.J.H. Brouwers, The hydration of slag, part 1: reaction models for alkali-activated slag, J. Mater. Sci. 42 (2) (2007) 428–443.
[31] JC/T 603-2004, Standard test method for drying shrinkage of mortar[S]. 2004.
[32] GB/T 17671-1999, Method of testing cement-determination of strength[S], 1999.
[33] J. Li, Q. Yu, H. Huang, et al., Effects of Ca/Si ratio, aluminum and magnesium on the carbonation behavior of calcium silicate hydrate, Materials 12 (8) (2019) 1268.
[34] E. L'Hôpital, B. Lothenbach, D.A. Kulik, et al., Influence of calcium to silica ratio on aluminium uptake in calcium silicate hydrate, Cem. Concr. Res. 85 (2016) 111–121.
[35] H. Zhou, X. Wu, Z. Xu, et al., Kinetic study on hydration of alkali-activated slag, Cem. Concr. Res. 23 (6) (1993) 1253–1258.
[36] S. Puligilla, P. Mondal, Co-existence of aluminosilicate and calcium silicate gel characterized through selective dissolution and FTIR spectral subtraction, Cem. Concr. Res. 70 (2015) 39–49.
[37] GB/T 208–2014, Test method for determining ce ment density[S], 2014.
[38] W. Kunther, Z. Dai, J. Skibsted, Thermodynamic modeling of hydrated white Portland cement–metakaolin–limestone blends utilizing hydration kinetics from ^{29}Si MAS NMR spectroscopy, Cem. Concr. Res. 86 (2016) 29–41.
[39] S.E. Ashbrook, K.J.D. MacKenzie, S. Wimperis, ^{27}Al multiple-quantum MAS NMR of mechanically treated Bayerite (α-$Al(OH)_3$) and silica mixtures, Solid State Nucl. Magn. Reson. 20 (3–4) (2001) 87–99.
[40] H. Dongshuai, W. Cong, Y. Qingrui, et al., Insights on the molecular structure evolution for tricalcium silicate and slag composite: from 29Si and 27Al NMR to molecular dynamics, Compos. Part B Eng. (2020), 108401.
[41] G.K. Sun, J.F. Young, R.J. Kirkpatrick, The role of Al in C–S–H: NMR, XRD, and compositional results for precipitated samples, Cem. Concr. Res. 36 (1) (2006) 18–29.
[42] K.J.D. MacKenzie, R.H. Meinhold, B.L. Sherriff, et al., ^{27}Al and ^{25}Mg solid-state magic-angle spinning nuclear magnetic resonance study of hydrotalcite and its thermal decomposition sequence, J. Mater. Chem. 3 (12) (1993) 1263–1269.
[43] K. Coenen, F. Gallucci, B. Mezari, et al., Investigating the role of the different metals in hydrotalcite Mg/Al-based adsorbents and their interaction with acidic sorbate species, Chem. Eng. Sci. 200 (2019) 138–146.
[44] T.T.H. Bach, C.C.D. Coumes, I. Pochard, et al., Influence of temperature on the hydration products of low pH cements, Cem. Concr. Res. 42 (6) (2012) 805–817.
[45] S.A. Bernal, Ruby Mejía de Gutiérrez, J.L. Provis, Engineering and durability properties of concretes based on alkali-activated granulated blast furnace slag/metakaolin blends, Constr. Build. Mater. 23 (2009) 99–108.
[46] Y. Zuo, M. Nedeljković, G. Ye, Coupled thermodynamic modelling and experimental study of sodium hydroxide activated slag, Constr. Build. Mater. 188 (2018) 262–279.
[47] G. Geng, R.J. Myers, M.J.A. Qomi, et al., Densification of the interlayer spacing governs the nanomechanical properties of calcium-silicate-hydrate, Sci. Rep. 7 (1) (2017) 1–8.
[48] G.K. Sun, J.F. Young, R.J. Kirkpatrick, The role of Al in C-S-H: NMR, XRD, and compositional results for precipitated samples, Cem. Concr. Res. 36 (1) (2006) 18–29.
[49] I.G. Lodeiro, D.E. Macphee, A. Palomo, et al., Effect of alkalis on fresh C–S–H gels. FTIR analysis, Cem. Concr. Res. 39 (3) (2009) 147–153.
[50] L. Pegado, C. Labbez, S.V. Churakov, Mechanism of aluminium incorporation into C-S-H from ab initio calculations, J. Mater. Chem. A 2 (10) (2014) 3477–3483.
[51] H. Ye, Creep mechanisms of calcium–silicate–hydrate: an overview of recent advances and challenges, Int. J. Concr. Struct. Mater. 9 (4) (2015) 453–462.
[52] E. Bernard, B. Lothenbach, C. Cau-Dit-Coumes, et al., Magnesium and calcium silicate hydrates, Part I: Investigation of the possible magnesium incorporation in calcium silicate hydrate (CSH) and of the calcium in magnesium silicate hydrate (MSH), Appl. Geochem. 89 (2018) 229–242.